Appl. Phys. B (2016) 122:141
DOI 10.1007/s00340-016-6403-2

Applied Physics B
Lasers and Optics

Time reversal versus adaptive optimization for spatiotemporal nanolocalization in a random nanoantenna

Dominik Differt[1] · Matthias Hensen[1] · Walter Pfeiffer[1]

Received: 22 September 2015 / Accepted: 1 April 2016 / Published online: 9 May 2016

Abstract Spatiotemporal nanolocalization of ultrashort pulses in a random scattering nanostructure via time reversal and adaptive optimization employing a genetic algorithm and a suitably defined fitness function is studied for two embedded nanoparticles that are separated by only a tenth of the free space wavelength. The nanostructure is composed of resonant core–shell nanoparticles (TiO_2 core and Ag shell) placed randomly surrounding these two nanoparticles acting as targets. The time reversal scheme achieves selective nanolocalization only by chance if the incident radiation can couple efficiently to dipolar local modes interacting with the target/emitter particle. Even embedding the structure in a reverberation chamber fails improving the nanolocalization. In contrast, the adaptive optimization strategy reliably yields nanolocalization of the radiation and allows a highly selective excitation of either target position. This demonstrates that random scattering structures are interesting multi-purpose optical nanoantennas to realize highly flexible spatiotemporal optical near-field control.

1 Introduction

Subwavelength localization of light and control of spatial and temporal properties of nanolocalized electromagnetic fields is of rather fundamental interest for future applications of photonics. For example, integration of photonics with microelectronics would benefit from overcoming the dimension gap between optical wavelengths on the μm scale and typical electronic device length scales in the order of some tenths of nanometers. Optical antennas and near-field distributions in their vicinity bridge this gap and are presently intensively investigated in nanophotonics (for a recent review see [1]). For example, coupling nanoscale waveguide structures [2] and manipulation of the directional emission characteristic of individual quantum systems [3] are demonstrated. Control of the near-field distribution in the vicinity of an optical antenna thus opens new fascinating possibilities for quantum control and spectroscopy, as it has been demonstrated recently in a theoretical investigation [4].

The application of ultrafast pulse excitation in combination with pulse shaping to control local fields was first proposed by Mark Stockman and coworkers [5]. The ability to control the spatial and temporal evolution of the optical near-field is greatly enhanced if the time-dependent polarization of the incident light is chosen as an additional degree of freedom as we have shown in theoretical investigations [6, 7]. In a first experimental step, we implemented spatial control below the diffraction limit using photoemission electron microscopy (PEEM) in combination with an adaptive learning algorithm [8]. This scheme could then be generalized toward simultaneous spatial and temporal subdiffraction ultrafast control of nanophotonic excitations, combining polarization pulse shaping and time-resolved PEEM [9]. It was possible to switch the location of excitation in the vicinity of a silver nanostructure by several tens of nanometers within several tens of femtoseconds.

An interesting alternative to the adaptive optimization of spatiotemporal optical near-field control is based on the time reversal symmetry of Maxwell's equations [10] or any

This article is part of the topical collection "Ultrafast Nanooptics" guest edited by Martin Aeschlimann and Walter Pfeiffer.

✉ Dominik Differt
pfeiffer@physik.uni-bielefeld.de

[1] Fakultät für Physik, Universität Bielefeld, Universitätsstr. 25, 33615 Bielefeld, Germany

other wave equation. The time reversal strategy was successfully realized with acoustic waves [11–13] and provides first applications in medicine and marine communications [14]. Later it was also experimentally demonstrated for radiofrequency (RF) fields [15, 16] and subwavelength focusing is realized [17].

A point-like emitter embedded in a complex subwavelength-scale scattering environment produces a complex outgoing wave in the far field. If this outgoing wave is time reversed, i.e., it is back-propagated to the emitter structure with the opposite spectral phase, the electromagnetic fields will relocalize at the original source in space and time [15, 16]. Most interestingly controlled energy localization well below the diffraction limit can be achieved, if near-field scattering occurs in the environment of the emitter [16, 17]. Several closely spaced radiofrequency antennas are individually embedded in a subwavelength scale (diameter $\approx \lambda/100$) random scattering environment composed of copper wire brushes. The emitted short electromagnetic pulses are distorted by the scattering environment. These outgoing waves are then multiply reflected from the walls of a metallic reverberation chamber surrounding the whole setup and picked up by several standard dipole RF receiver antennas. The electronically recorded signals are time reversed and then reemitted from these receiver antennas. The so created back-propagating wave relocalizes at the original emitter antenna with a spatial selectivity of about $\lambda/30$. The scheme allows addressing individual RF antennas that are spatially separated well below the diffraction limit. This demonstrates that the time reversal scheme could replace adaptive optimization schemes with the benefit that no time-consuming learning algorithm is required.

The demonstration of subwavelength localization of RF fields is of particular interest for future applications of coherent control schemes with optical nanoantennas. Being demonstrated with RF waves the time reversal control scheme might also work at optical frequencies. If the localization efficiency demonstrated for radiofrequencies can be also reached in the visible spectrum radiation, energy localization on the scale of several tens of nanometers might be feasible. In the following this is referred to as nanolocalization of electromagnetic fields. Several theoretical investigations demonstrate the applicability of the scheme [18–21], but an experimental demonstration is still missing. On a very fundamental level, it was shown that for a non-absorbing scattering medium time reversal is equivalent to reciprocity and thus makes nanolocalization of time-reversed fields possible [18, 19]. The analysis is based on a perfect time reversal mirror (TRM), i.e., all outgoing planar wave components are recorded and time reversed. Both, the realization of a perfect TRM as well as the lossless scattering medium are challenging requirements for the experimental realization of the time reversal control scheme at optical frequencies. Presently it is an open question under which conditions nanolocalization of time-reversed optical fields can be expected.

In the RF time reversal experiment [17], the reverberation chamber plays an important role to direct the outgoing wave components from the emitter antenna at different time delays to the TRM receiver antennas. This concept is not directly applicable at optical frequencies because of the required small size of the reverberation chamber ($\approx 10\lambda$). Conceptually the reverberation chamber can be conceived as a resonator. Incorporating suitable resonator functionality in the random scattering nanoantenna itself could overcome the necessity for an encompassing reverberation chamber as it was demonstrated for a random two-dimensional metallic nanostructure [21]. This finding is relevant with respect to an experimental realization of the time reversal scheme since it demonstrates that not the whole outgoing wave has to be time reversed in order to observe nanolocalization and, in addition, that the concept works also with some loss in the scattering medium. This theoretical simulation of time reversal focusing in the optical frequency regime is promising but is not based on a realizable design of the near-field scattering structure. The structure is two-dimensional and the transducer is selected not by chance. Instead it is carefully chosen by searching the most promising modes that couple the near-field to the far field. In addition, the efficiency of the time reversal algorithm is not assessed in this investigation.

Here we investigate nanolocalization in a three-dimensional random scattering nanostructure composed of randomly sized core–shell nanoparticles placed at random positions in space. Hence emitter positions in the nanostructure are chosen without bias and do not exhibit for example an extraordinarily high coupling to far-field modes. Two closely positioned emitter particles in the nanostructure allow investigating the nanolocalization selectivity. In addition to the nanolocalization via time reversal adaptive optimization is applied to obtain an estimate for the best possible nanolocalization in the given nanostructure. This serves as reference for comparison with the nanolocalization achieved via time reversal. For the given nanostructure, time reversal fails as universal scheme for nanolocalization and in all cases the adaptive optimization yields significantly improved localization selectivity. Differences in the behavior of the two different emitters indicate that the localization efficiency is determined by coupling of the emitter to a particular local mode in the nanostructure that is then addressed by plane wave far-field illumination.

The paper is structured as follows: In Sect. 2 the scattering structure and the methodology for field calculations, time reversal and adaptive optimization using a genetic algorithm are summarized. The comparison of

nanolocalization achieved by both strategies is presented in Sect. 3 for different illumination conditions. The general rules derived from the reported observations are summarized and discussed in Sect. 4.

2 Random scattering structure and methodology

2.1 Response calculation for scattering nanostructure

Calculations are performed by multiple elastic scattering of the multipole expansion (MESME) method [22]. Scattered fields are expanded in spherical harmonics, providing the most natural basis for spherical scattering problems. In an iterative scheme, the self-consistent field distribution is obtained. The number of iterations and the maximum multipole order of the individual scattered fields are chosen to ensure convergence of the calculations. The advantage of the approach for the given studied system, i.e., a random assembly of non-intersecting spheres, is that the field can be calculated at any location outside of the spheres. In addition, no artifacts because of the discretization of the nanostructure influence the calculated field distributions as they for example arise as staircasing artifacts in FDTD modeling, i.e., spurious field maxima induced by the step-like representation of curved interfaces.

For the random scattering nanostructure embedded in a reverberation chamber, the MESME algorithm is not applicable and we turned to a commercial FDTD package (Lumerical) to solve Maxwell's equations for the given geometry. In order to minimize staircasing artifacts at the nanoparticle surface the scattering structure is surrounded by an additional mesh (240 nm × 150 nm × 150 nm) of 1 nm resolution in each direction. Core–shell particle radii vary from 24 to 25 nm, and the respective dielectric properties are modeled by an effective refractive index [23] to match single particle resonances to MESME results and to avoid thin particle shells in the FDTD calculations. As discussed below in more detail, the size of the core–shell particles is chosen to support resonances in the frequency range between 2.35 rad fs^{-1} (800 nm) and 2.69 rad fs^{-1} (700 nm). The duration of the simulation was set to 300 fs so that the intensity of the electric fields outside the chamber has dropped by nearly two orders of magnitude with respect to highest intensities at the beginning of the simulation. Illumination from far field is realized with a total-field scattered-field source which encloses whole structure. This method is superior to extended plane wave sources since no additional energy is injected into the simulation by diffraction at the confining perfectly matched layer boundary conditions.

2.2 Characterization of random scattering nanostructure

The structure of the random nanoscale scattering structure investigated here is shown schematically in Fig. 1a. It consists of spherical nanoparticles that are randomly placed in three dimensions. Interestingly, it is conceivable that such kind of structures can form by chance in a random agglomeration process. Embedded in the random nanoscale scattering structure are two emitter particles denoted *red* and *blue* with centers separated by 80 nm. Hence, these emitter particles are separated by $\lambda/10$ and it is the scope of the present investigation to study whether the time-reversed fields originally emitted from emitter *red* or emitter *blue* nanolocalize again at the corresponding emitter.

The nanoscale scattering environment of the emitter particles consists of ten randomly placed nanoparticles of varying radius between 24.1 and 25 nm. The surrounding nanoparticles are randomly placed within two spheres with predefined equal radii centered at the two emitter nanoparticles. The chosen positions obey the constraint that the gap between neighboring particles is larger than 0.6 nm. Both the emitters and the particles in the scattering environment are core–shell particles composed of a TiO_2 core with 21 nm radius and Ag shell of the remaining thickness. For the calculations, a wavelength independent relative permittivity $\varepsilon = 6.35$ and the optical properties of Johnson and Christy [24] are used for the titanium dioxide core and the Ag shell, respectively. The variation of the particles size causes a spectral shift in the SPP eigenmodes of the individual core–shell particles in the range between 2.35 rad fs^{-1} (800 nm) and 2.69 rad fs^{-1} (700 nm) as it is seen in the corresponding total scattering cross sections (colored lines in Fig. 1b). The total scattering cross section of the whole nanoparticle aggregate exhibits a rather complex spectrum (black solid and dotted line in Fig. 1b) with different features, i.e., effects related to plasmon polariton dimerization and the occurrence of extended plasmon modes involving more than two particles. The spectral features in the total scattering cross section in the range between 2.22 rad fs^{-1} (850 nm) and 2.51 rad fs^{-1} (750 nm) are attributed to single particle and dimer-like resonances. Upon dimerization the bright plasmon mode, i.e., the mode visible in the total scattering cross section, shifts to the red. This is shown in Fig. 1b by reducing the gap a of a dimer formed by two identical particles (radius 25 nm) from 100 to 1 nm (gray shaded curves). A histogram over all appearing dimer gap sizes a appearing inside of the scattering structure is shown in Fig. 1c. They were identified by processing all connection lines from every particle center to every other. All connections without any third particle intersecting are counted as a dimer

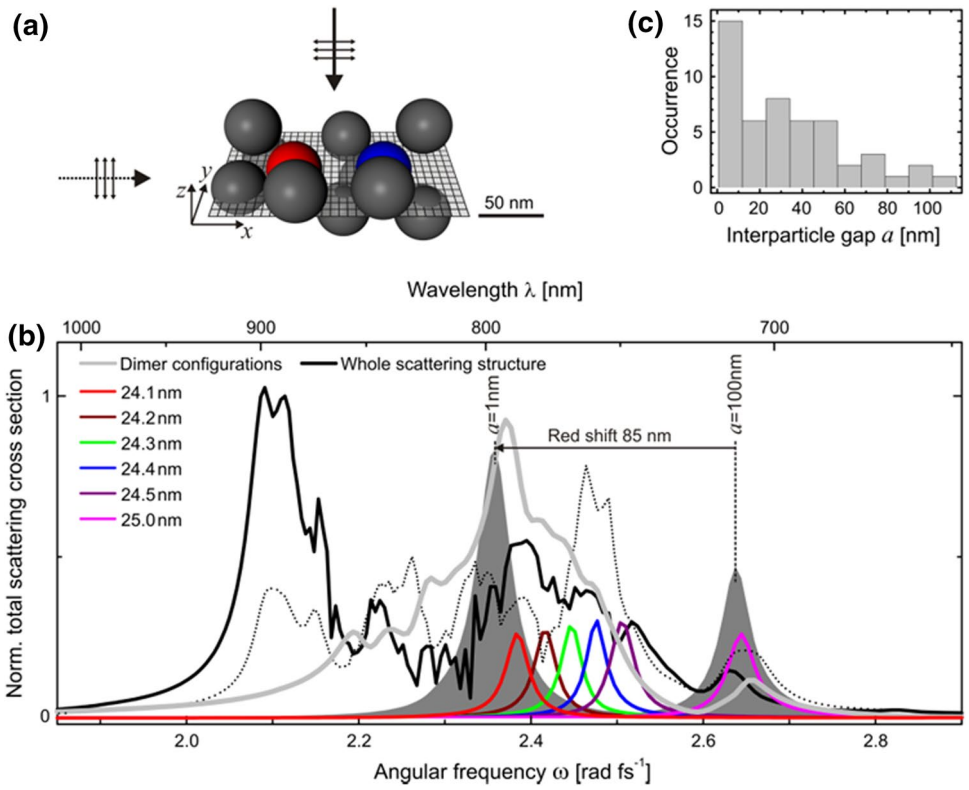

Fig. 1 Random scattering structure. **a** Schematic representation of scattering structure. The *grid* indicates the plane for which fields were calculated. The emitter particles are shaded in *blue* and *red*. The origin of the coordinate system is in the center between both emitters and the shown coordinate system axes are displaced from the origin for reasons of clarity. **b** Total scattering cross section of single core–shell particles with different outer radii (*colored curves*), the coherent sum core–shell particle dimers with different interparticle gaps a (*gray filled curves*), the dimer-like scattering contribution obtained as coherent sum of scattering amplitudes of the various dimer configurations (*gray line*, details in the text), and the scattering cross section of the whole structure for light incidence parallel to the x axis (*dotted black line*) and parallel to the z axis (*solid black line*). **c** Histogram of dimer gaps identified for the random scattering structure shown in **a**

and the corresponding total scattered fields for the dimer alone were calculated. By coherent superposition of the scattering fields of all dimer configurations of the scattering structure, one obtains the dimer induced total scattering cross section for illumination with light incident parallel to the z axis and polarized in x-direction (gray line in Fig. 1b). It contains the scattering amplitudes solely of the dimers and is composed of contributions in the range from 2.15 rad fs^{-1} (875 nm) to 2.51 rad fs^{-1} (750 nm), i.e., somewhat red-shifted with respect to the resonances of the individual particles. The total scattering cross section of the whole structure itself is shown for light incident parallel to the z axis (solid black line in Fig. 1b) and parallel to the x axis (dotted black line in Fig. 1b), with polarizations along the x- and z-direction, respectively. The comparison of the dimer-related scattering cross section and scattering cross section of the whole structure one finds contributions around 2.10 rad fs^{-1} (≈900 nm) that cannot be attributed to dimerization. These contributions are assigned to higher order plasmonic excitations that involve excitations of more than two nanoparticles.

The qualitative analysis of the scattering spectrum shows that the interaction between nanoparticles plays an important role for the presently chosen random scattering structure. As a consequence, the total spectral width of the scattering spectrum is much wider than the sum of the scattering spectra of the individual nanoparticles and hence the whole spectral range should be involved in the time reversal process. Modern laser systems provide pulse durations in the few-cycle regime covering the spectral range of more than an octave. Therefore, the requirement to cover a broad spectral range does not restrict the experimental realization. It is interesting to note that the scattering spectrum exhibits qualitative similarities to acoustic modes of a distribution of bubbles for which the time reversal concept was recently investigated [25].

2.3 Time reversal strategy for nanolocalization

The principle of the time reversal algorithm is shown in Fig. 2. First a 5 fs short bandwidth-limited light pulse with a Gaussian spectrum is emitted by either emitter *red* or *blue*

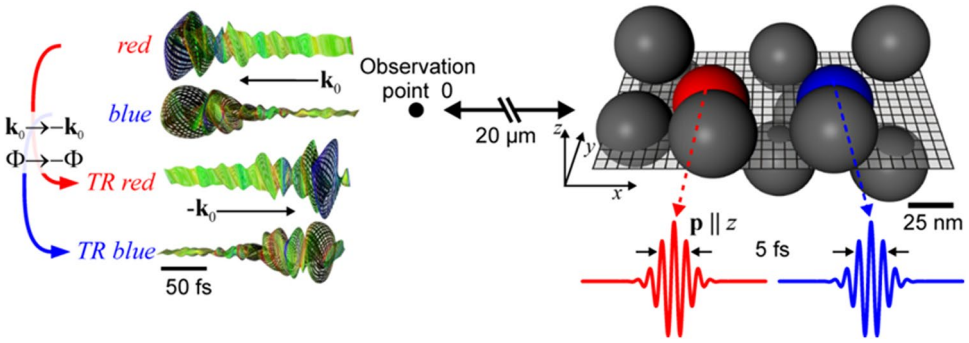

Fig. 2 Time reversal of electromagnetic fields. From each of the embedded emitters, a 5 fs Gaussian light pulse is emitted and the spatial and temporal pulse profile is heavily distorted by the random scattering structure. In the far field at observer point 0, 20 µm away from the scattering structure, the scattered pulses *red* and *blue* are calculated for light emitted from both emitters. Both emitters radiate at the same frequency. The emitter dipoles $\mathbf{p}$ are oriented parallel to the z axis. By applying the time reversal transformation $\mathbf{k}_0 \rightarrow -\mathbf{k}_0$ and $\Phi_{red/blue}(\omega, \mathbf{k}_0) \rightarrow -\Phi_{red/blue}(\omega, \mathbf{k}_0)$, i.e., their spectral phases are replaced by the negative phase and the direction of propagation is reversed, yielding the time-reversed fields *TR red* and *TR blue*. The spectral phase is given by $\Phi_{red/blue}(\omega, \mathbf{k}_0) = Arg\left(\mathbf{E}_{red/blue}(\omega, \mathbf{k}_0)\right)$

with a dipole moment orientated parallel to z axis. Note that the color coding differentiates the two different emitters that emit the same spectrum. In the absence of surrounding scatterers, a dipole-like emission pattern evolves in space and time. For emitters embedded in the nanostructure, the pulse undergoes multiple scattering by the surrounding particles and the emitter particles itself. The emitter particles participate in this multiple scattering process, i.e., the emitters are modeled as real particles. In this multiple scattering, many different plasmonic modes are excited and contribute to the far field pattern at observation point *O*. The observation point is chosen 20 µm away from the scattering structure to ensure that near-field contributions are negligible and that the local field can be well approximated by plane waves originating from the center of the scattering structure. In addition, the distance of the observation point from the random nanoantenna is large with respect to the nanoantenna size (250 nm) and thus the emitter can be regarded in good approximation as a point-like source. Therefore, the outgoing plane wave components can be reconstructed from the recorded time-dependent electromagnetic field at point *O*. In a similar way the amplitudes of outgoing plane wave components $\mathbf{k}(r, \vartheta, \varphi)$ in all directions can be determined. The scattered far-field pulse of emitter *red* and *blue* is shown in the time domain in an elliptical 3D representation [26]. In the time domain, the pulse shape is dominated by a ballistic part followed by an exponentially decaying scattering contribution, both exhibiting fast changes in polarization. In the spectral amplitude (Fig. 3, upper part), distinct sharp peaks on top of a broad background appear for both pulses and both polarization components. This indicates that the spectral resonances seen in the scattering cross section (Fig. 1b) influence the outgoing wave. Obviously particular plasmonic resonances in the scattering structure efficiently channel the energy

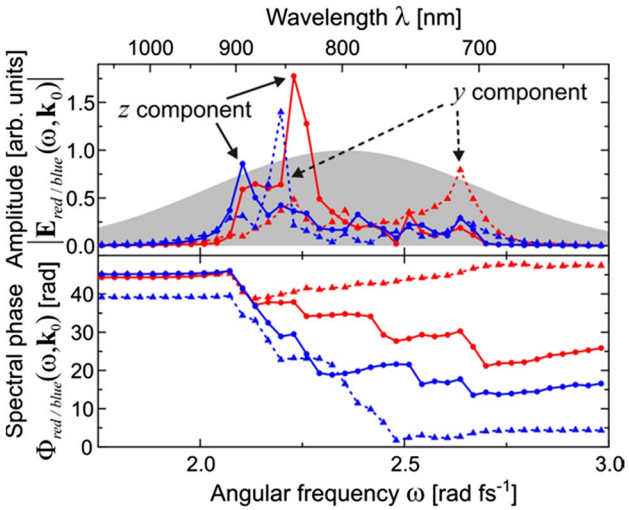

Fig. 3 Spectral amplitude and phase for polarization components in y-direction (*triangles*) and z-direction (*filled circles*) of the scattered light fields recorded at the observation point 0 defined in Fig. 2. The colors of the *symbols* reflect the origin of the pulse from either the *blue* or the *red* emitter. The spectrum of the originally emitted pulses is shown as *gray shaded area*. The spectral phase is shown for reasons of completeness but not further discussed in the text

into the far field. Interestingly some resonances appear for both emitters and some resonances are characteristic for a particular emitter.

Time-reversed fields $\mathbf{E}^{TR}_{red/blue}(\omega, \mathbf{k}_0)$ of the outgoing waves $\mathbf{E}_{red/blue}(\omega, \mathbf{k}_0)$ emitted from either emitter *red* or *blue* are obtained by reversing the $\mathbf{k}$-vectors of the wave packets and by sign inverting their spectral phases:

$$\mathbf{E}^{TR}_{red/blue}(\omega, \mathbf{k}_0) = \left| \mathbf{E}_{red/blue}(\omega, -\mathbf{k}_0) \right| e^{-i\,\Phi_{red/blue}(\omega, -\mathbf{k}_0)}. \quad (1)$$

According to the principle of nanolocalization via time reversal, the complex modulation of the time-dependent field amplitude and phase carries the information to accomplish the refocusing of the light pulses at their source emitter. To obtain the electromagnetic field within the scattering structure, we use the Green's function formalism in frequency domain. On each grid point $\mathbf{r}_i$ of the grid shown in Fig. 1a, the response function $\tilde{\mathbf{S}}(\mathbf{r}_i, \omega, \mathbf{k}_0)$ [27] is determined via a MESME calculation by Green's function formalism for incident plane waves $\mathbf{k}_0$ and both polarization components. Note that the index related to the polarization component is omitted for clarity. The local field $\mathbf{E}^{local}_{red/blue}(\mathbf{r}_i, \omega, \mathbf{k}_0)$ is then obtained via

$$\mathbf{E}^{local}_{red/blue}(\mathbf{r}_i, \omega, \mathbf{k}_0) = \tilde{\mathbf{S}}(\mathbf{r}_i, \omega, \mathbf{k}_0)\ \mathbf{E}^{TR}_{red/blue}(\omega, \mathbf{k}_0), \tag{2}$$

where summation over both polarization components is implied.

2.4 Adaptive optimization of nanolocalization

To evaluate the localization efficiency of time-reversed fields, quantitative knowledge of the best possible localization is needed, since it is not guaranteed that the time reversal scheme yields the optimum nanolocalization. For a given spectral distribution, it is conceivable that a particular spectral phase might yield even better field localization compared to the time-reversed fields. Since there exists no analytical method to determine the spectral phase leading to the best possible localization, we apply an adaptive optimization scheme as it has been demonstrated already in previous studies [6–8]. Here we use a genetic algorithm method to find spectral phases for both polarization components with optimum localization efficiency. To implement the genetic algorithm, the optimization goal has to be defined as a fitness function. Depending on the chosen fitness function, the algorithm will find different optima. Details about the applied fitness functions are discussed below. Note that the genetic algorithm cannot guarantee finding the global optimum since the number of generations is limited but nevertheless a larger parameter space is probed compared to simple gradient-based optimization strategies and the chance of being trapped in local minima can be reduced.

The nanolocalization efficiency is imprinted both in the spectral amplitude and the spectral phase of the back-propagated wave. To allow comparison between adaptively optimized localization and time-reversed fields, we apply pure phase shaping. The genetic algorithm optimizes the 100 sampling points of the spectral phase for each polarization component using a Taylor expansion. In case of illumination with plane wave from different directions, the spectral phases for each direction are treated independently, i.e., the parameter space increases linearly with the number of illumination directions.

2.5 Determination of nanolocalization and selectivity

Both nanolocalization strategies require a measure for the achieved nanolocalization and selectivity in addressing the original emitter. To achieve this, the fluence localization selectivity $S^{red/blue}_{TR/AO}$ is defined according to the procedure described below.

The local fluence $f_j(\mathbf{r}_i)$ on the above defined grid $\mathbf{r}_i$ in the random nanostructure is calculated from the local field $\mathbf{E}^{local}_j(\mathbf{r}_i, \omega, \mathbf{k}_0)$ via

$$f_j(\mathbf{r}_i) = \sum_{\omega} \left| \mathbf{E}^{local}_j(\mathbf{r}_i, \omega, \mathbf{k}_0(\omega)) \right|^2. \tag{3}$$

Note that f_i is not a fluence in the classical meaning for transverse electromagnetic waves. It is just a quantity that is proportional to the integral of the time-dependent local energy intensity. The lower index j indicates whether the time-reversed fields derived from the fields originally emitted from either emitter *red* or *blue* or adaptively optimized (*AO*) fields for emitter *red* and *blue* are considered ($j = TR\ red$, $TR\ blue$, $AO\ red$, $AO\ blue$). The spatially selective light localization on one of the emitters is then defined by the quotient of two spatially averaged fluences as shown in Fig. 4a, b, for refocusing on the emitters *red* and *blue*, respectively. The local fields vary significantly and thus some spatial averaging is needed to obtain a reliable measure of the field localization. Hence, in a circle around emitter *red*, the fluence is averaged over the red-colored grid points indicated in Fig. 4a and denoted $\langle f^{red}_j \rangle$. The analog definition is used to calculate the average fluence localized at the blue emitter $\langle f^{blue}_j \rangle$ and the averaged fluence ending up in the remaining nanostructure $\langle f^{residual}_j \rangle$. The lower index again indicates which strategy is applied for nanolocalization on which emitter. The rather coarse grid leads to substantial variations of the local fields recorded at neighboring grid positions. However, this does not significantly affect the average fluences $\langle f_j \rangle$ since they are obtained as averages over a sufficiently large ensemble of grid points.

As a measure for the degree of spatial nanolocalization at either emitter *red* or *blue*, we introduce the fluence ratio

$$F^{red/blue}_j = \frac{\left\langle f^{red/blue}_j \right\rangle}{\left\langle f^{residual}_j \right\rangle}. \tag{4}$$

As there are two emitters we define an additional parameter to quantify the selectivity of fluence localization. This

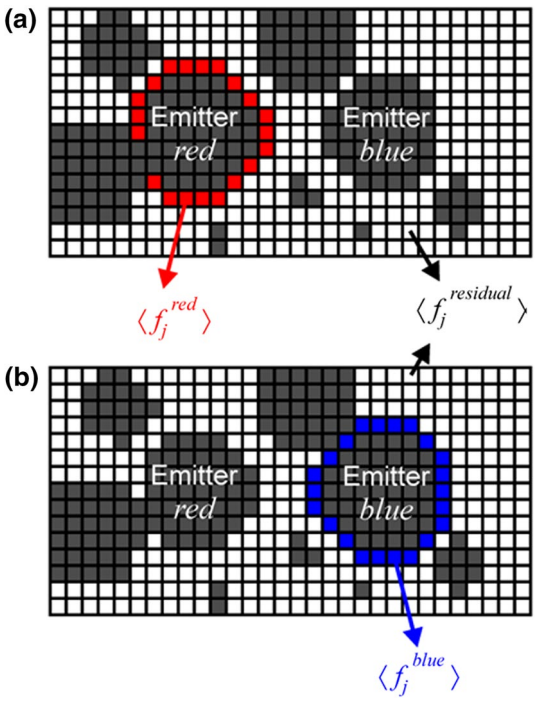

Fig. 4 Definition of the spatially averaged fluences. The *colored* grid points are situated on a *circle* with about 32 nm radius. *White* grid points are outside of the *circle*. Grid points inside of core shell particles are grayed out. Part **a** and **b** correspond to the definition for emitter *red* and *blue*, respectively. Note that the grid is too coarse to resolve the non-intersecting nanoparticles leading to seemingly coalescing particles. The grid points are situated in the center of each grid square, and the distance between neighboring grid points is 6.7 nm in both *x*- and *y*-direction

is critical if the nanolocalization scheme is applied to direct energy or information, as it was for example demonstrated for RF pulses [17], selectively to either emitter *red* or *blue*. The localization selectivity ratios $S_{TR}^{red/blue}$ of interest are defined as

$$S_{TR}^{red} = \frac{F_{TR\,red}^{red}}{F_{TR\,red}^{blue}}, \quad S_{TR}^{blue} = \frac{F_{TR\,blue}^{blue}}{F_{TR\,blue}^{red}},$$
$$S_{AO}^{red} = \frac{F_{AO\,red}^{red}}{F_{AO\,red}^{blue}} \text{ and, } \quad S_{AO}^{blue} = \frac{F_{AO\,blue}^{blue}}{F_{AO\,blue}^{red}}. \tag{5}$$

If, for example, $S_{TR}^{red} > 1$ is fulfilled, more energy is directed toward emitter *red* than toward emitter *blue* for illumination of the random nanostructure with the time-reversed field derived from the field emitted from emitter *red*. A large value of S_{TR}^{red} indicates strong nanolocalization at emitter *red* since this is only achieved if a small amount of energy reaches emitter *blue*, i.e., F_{TRred}^{blue} is small. Hence, a highly selective excitation is achieved if both selectivity ratios, $S_{TR/AO}^{red}$ and $S_{TR/AO}^{blue}$, are large.

3 Results

As mentioned in the introduction, the nanolocalization is influenced by the degree to which the complete outgoing distorted wave can actually be time-reversed. In principle all outgoing partial waves in all three-dimensional directions need to be recorded and time-reversed. The treatment of the full three-dimensional scattered-field distribution is beyond the scope of the present investigation. Here, we restrict the analysis of nanolocalization via time reversal to plane wave and approximate cylindrical wave illumination to study how the superposition of time-reversed illumination from different directions influences the nanolocalization.

3.1 Fluence nanolocalization for unidirectional plane wave illumination

The spatially resolved fluence for the back-propagated time-reversed pulse from emitter *red* and *blue*, denoted in the following *TR red* and *TR blue*, are shown in the upper part of Fig. 5. The illumination conditions chosen here correspond to the situation depicted in Fig. 2. Already with the naked eye the preferential nanolocalization at the corresponding emitter particle is obvious. Upon illumination with *TR red*, the fluence in the vicinity of emitter *red* is enhanced in comparison with emitter *blue*. In addition, for *TR blue* the fluence is concentrated around emitter blue. This indicates that the time reversal strategy is in principle capable of switching spatial fluences on a subwavelength scale. However, an assessment of the nanolocalization efficiency requires a quantitative measure of nanolocalization and the comparison with an alternative nanolocalization strategy. Note that the fluence distribution shown in Fig. 5 contains only information on the spatial energy concentration and not about the time evolution of the nanolocalized field distribution. The latter aspect is discussed below.

In addition to the time reversal strategy for nanolocalization, a genetic algorithm has been used. As seen in Fig. 3, the far-field spectra for both emitters vary significantly and differ significantly from the original Gaussian. Hence, the spectral composition will strongly influence the ability for nanolocalization. Hence, to allow direct comparison of both nanolocalization strategies, the same spectral amplitudes as used for time reversal are also used for adaptive optimization. The spectral shape for both polarization components is kept constant, while the spectral phase was optimized to achieve the optimal enhancement of the localization selectivity ratio $S_{AO}^{redblue}$. For the optimum pulse shape, the spatially resolved fluence $f_{AO\,red}(\mathbf{r}_i)$ and $f_{AO\,blue}(\mathbf{r}_i)$ are shown in the lower part of Fig. 5. In

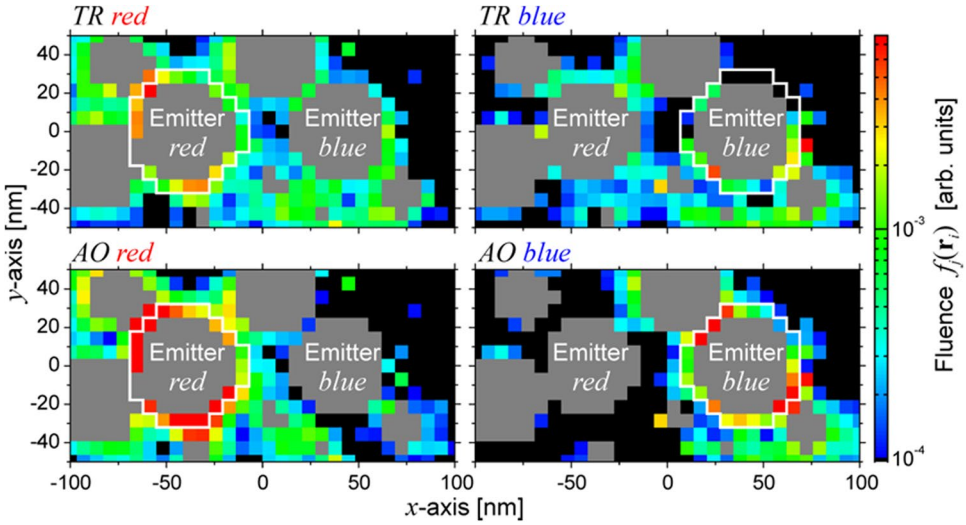

Fig. 5 Comparison of exemplary fluence distributions $f_j(\mathbf{r}_i)$ obtained via time reversal (*upper row*) and adaptive optimization (*lower row*) for emitter *red* and *blue*. The fluence distribution is represented on a log scale to cover the large contrast. The *white line* borders the grid points that are inside a 32 nm radius around the emitter. Grid points overlapping with nanoparticles are grayed out. The shown distributions correspond to the far fields recorded at the observation point located at position (−20,0,0) µm

comparison with the time reversal algorithm, the fluence is much better localized at the emitter particle and in additional the fluence on the inactive emitter is drastically reduced.

The quantities introduced in Sect. 4 can now be applied to quantify the nanolocalization efficiency and selectivity. The fluence ratios $F_j^{red/blue}$ for the fluence distributions $f_j(\mathbf{r}_i)$ are graphically represented in Fig. 6. The fluence ratios achieved via time reversal are shown in the upper picture. Compared to the average fluence of the *TR red* pulse, the fluence localization is enhanced at emitter *red* by a factor 5.5, i.e., F_{TRred}^{red} is 5.5. In contrast, F_{TRred}^{blue} is about unity and hence the corresponding color bar overlaps with the dashed line indicating the average fluence in Fig. 6. The situation reverses for the *TR blue* pulse and the light is now preferentially localized at emitter *blue*. The calculated selectivity ratios are above unity in both cases and thus preferential energy nanolocalization to either emitter nanoparticle is achieved by the TR scheme.

However, this does not yet demonstrate that the time reversal strategy is indeed responsible for the nanolocalization since spectral filtering could also explain the preferential nanolocalization. A possibility to check for the impact of the spectral phase on the nanolocalization is to compare the time-reversed field distribution with the distribution obtained for a constant phase of the back-propagated pulses, i.e., illumination with bandwidth limited pulses. This yields the selectivity ratios for bandwidth-limited illumination $S_{const,phasered}^{red} = 2.55$ and $S_{const,phaseblue}^{blue} = 3.34$ for localization at emitter *red* and *blue*, respectively. For emitter *red*, the selectivity is reduced by more than a factor two, whereas for emitter *blue* the selectivity is even increased by about 50 %. This ambiguous behavior indicates that the phase of the time-reversed fields has some relevance

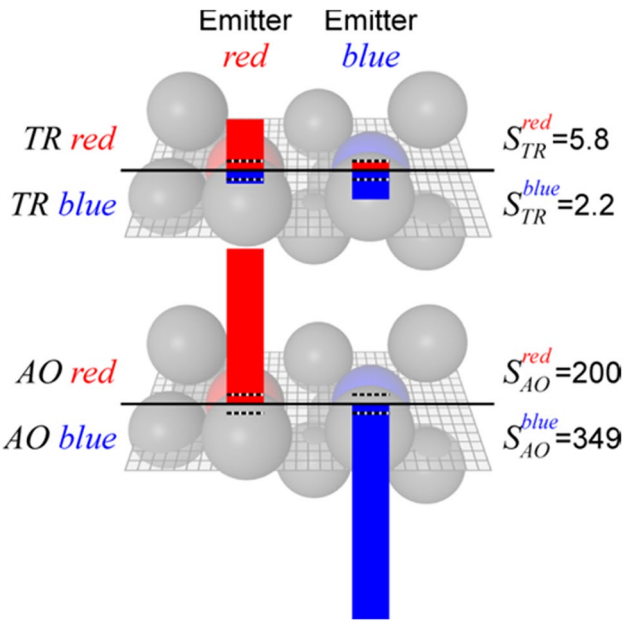

Fig. 6 Fluence ratios $F_j^{red/blue}$ and selectivity ratios $S_{TR/AO}^{red/blue}$ corresponding to the fluence distributions shown in Fig. 5. The size of the *bars* are scaled proportional to the fluence ratios $F_j^{red/blue}$ normalized to the average residual fluence $\langle f_j^{residual} \rangle$ depicted as *black dotted lines*

for nanolocalization but other mechanism might have a stronger influence.

A second critical test of the time reversal strategy is the application of an alternative nanolocalization strategy that is in principle able to determine the optimal nanolocalization for a given illumination spectrum. As optimization goal a maximized localization selectivity ratio was chosen. Interestingly, the adaptively optimized pulses *AO red* and *AO blue* (Fig. 6, lower part) both show a very high fluence

ratio. The fluence on the inactive emitter $\langle f_j^{red/blue} \rangle$ is much smaller than the average value $\langle f_j^{residual} \rangle$, while the localization on the active emitter $\langle f_j^{red/blue} \rangle$ is much stronger compared with time reversal. Consequently, the selectivity ratios are enhanced by nearly two orders of magnitude. The origin for this striking selectivity enhancement is not yet understood. Seemingly the random nanoantenna provides very efficient channels to direct the energy to a particular location inside the structure. Resolving the mechanism requires more studies systematically varying the coupling inside the nanostructure that lie beyond the scope of the present investigation. Note that there is no guarantee that the adaptive optimization algorithm used here indeed yields the global optimum since the evolution can only be executed for a limited number of generations. Thus, the optimum nanolocalization might even be further improved compared to the values given in Fig. 6.

For the given illumination direction, both localization strategies work and selectivity ratios above unity are obtained for both emitters. Hence, a selective nanolocalization of radiation on a subwavelength scale can be achieved in the nanostructure. However, the contrast ratio obtained for adaptive nanolocalization is almost two orders of magnitude larger.

3.2 Spatiotemporal nanolocalization for unidirectional plane wave illumination

We will now discuss the spatiotemporal nanolocalization by analyzing the temporal evolution of the local intensity profile in the vicinity of the emitter positions. The time reversal strategy should not only redirect the energy flow toward the original emitter but also the original time-structure of the emitter pulse should be reestablished. This is directly accessible for the time reversal algorithm as the temporal field evolution can be achieved by Fourier transformation of the frequency domain representation of the local field given in Eq. 2.

Again adaptive optimization is used to compare the achieved spatiotemporal nanolocalization. To maximize the local field strength, the fitness function must be based on a quantity that favors high local intensities. This is achieved by using the nonlinear local fluence $f_j^{nl}(\mathbf{r}_i)$ defined as

$$f_j^{nl}(\mathbf{r}_i) = \int \left| FT\left\{ \mathbf{E}_j^{local}(\mathbf{r}_i, \omega) \right\} \right|^4 \mathrm{d}t, \tag{6}$$

with FT representing the Fourier transform. As fitness function for adaptive optimization again the selectivity ratio defined by Eqs. 4 and 5 is used, but now calculated based on the nonlinear fluence (Eq. 6) instead of the linear fluence (Eq. 3). The time-dependent local intensity is shown in Fig. 7, both for time reversal (Fig. 7a, g) and adaptive optimization (Fig. 7b, h) for two representative positions in the vicinity of the emitters. For comparison, the bandwidth-limited temporal representation, i.e., the local field intensity evolution assuming constant spectral phase $Arg\left(\mathbf{E}_{red/blue}^{local}(\mathbf{r}_i, \omega)\right)$, is shown for each position. Zero padding has been applied to smooth the temporal intensity evolution. The *TR red* pulse induces a short pulse at emitter *red* but also at emitter *blue* the temporal intensity profile is almost bandwidth limited. In contrast the *TR blue* pulse generates an almost bandwidth-limited pulse on emitter *blue*, while the temporal intensity on emitter *red* is rather smeared out. Note that the intensity ratios for the time-dependent intensities for single positions in the vicinity of emitter *red* and *blue* do not reflect the average fluence ratios shown in Fig. 6 since no spatial averaging is taken into account. With respect of the time reversal strategy, it is important to note that the behavior shown in Fig. 7a, g is as expected. According to the time reversal scheme, the back-propagated pulse should spatiotemporal nanolocalize. Other parts of the scattering nanostructure should exhibit a rather unrelated behavior, i.e., the local field might also be concentrated in the time domain or not.

However, beyond the pure nanolocalization in space and time domain, the contrast of nonlinear fluences is of interest for nanoscale nonlinear optical switching. In this respect, the adaptive optimization scheme exhibits a clear advantage compared to the time reversal. The adaptive optimization strategy managed to induce an almost bandwidth-limited pulse at the target emitter and effectively smears out the temporal intensity profile at the other emitter yielding a significantly increased quadratic switching ratio. Note that this is imprinted by the choice of the fitness function. Obviously the random nanostructure is well-suited to match this target and thus offers interesting opportunities for future nonlinear optical switching devices.

Both adaptive optimization and time reversal yields local intensity transients at the original emitters that are almost bandwidth limited. In that respect, both nanolocalization strategies show little difference. However, since the adaptive scheme used directly the nonlinear selectivity ratio for optimization, somewhat lower intensities are obtained at the other emitter.

3.3 Impact of illumination direction on degree of time reversal nanolocalization

Up to now only one observation point and hence also illumination direction was considered. The emission patterns of the many SPP resonances are different and the far field in one particular scattering direction consists of contributions from different resonances inside the scattering structure. Those spectral features contain the information one needs to address the SPP resonances by illumination with the far field. This raises the question how the illumination direction affects the spatiotemporal nanolocalization by time reversal. Following the argumentation, one would expect

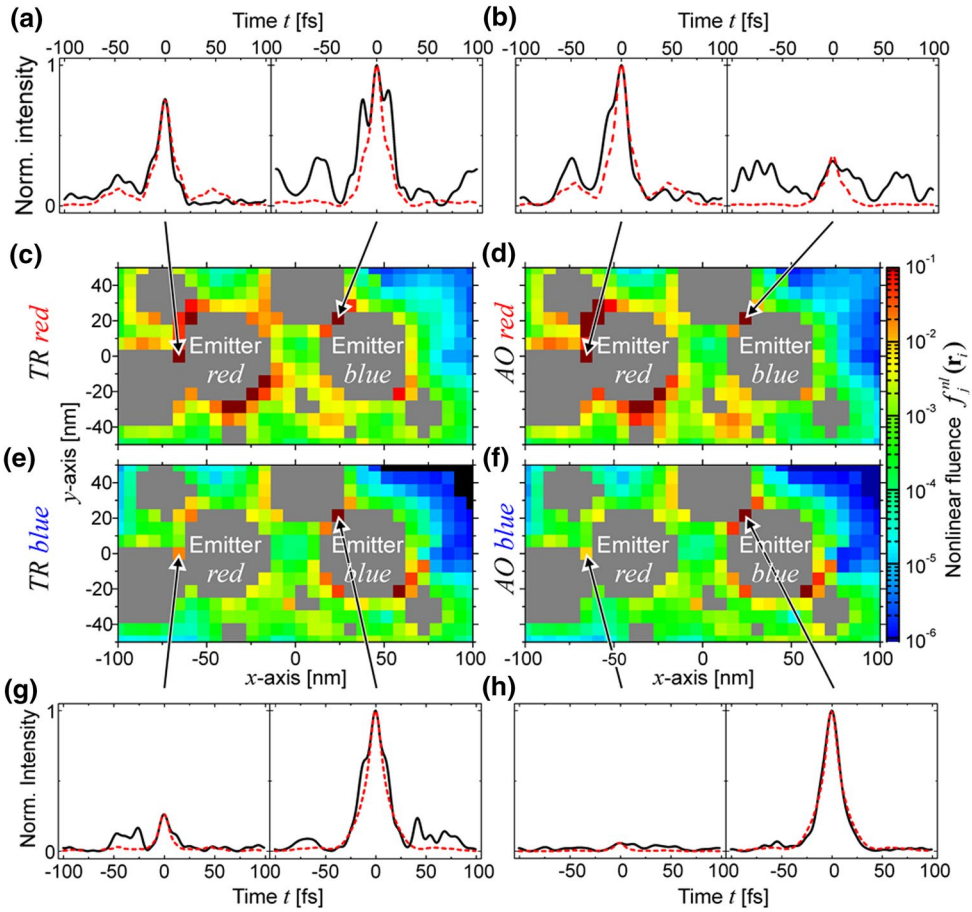

Fig. 7 Local time-resolved intensity (**a**, **b**, **g**, **h**) and local nonlinear fluence distribution (**c**, **d**, **e**, **f**) for nanolocalization via time reversal (part **a**, **c**, **e**, **g**) and adaptive optimization (part **b, d, f, h**) for plane wave illumination from *x*-direction. For two representative points in the vicinity of each emitter as indicated by *arrows*, the time-dependent intensity is shown for time reversal (**a**, **g**) and adaptive optimization (**b**, **h**) normalized to the maximum peak intensity in *each panel*. For comparison, the bandwidth-limited local field intensity is shown as *red dashed line* normalized to each corresponding intensity *curve*

differences in the efficiency of the time reversal algorithm by using other plane wave illumination directions.

To address those questions, we have repeated the refocusing by time reversal for ten different observation points corresponding to 10 different illumination directions $k_l (l = 0, 1, \ldots 9)$ in the *x*–*y*-plane as indicated in Fig. 8a. For each observation point, the scattered outgoing field amplitudes and the corresponding time-reversed fields were determined as described above. Similarly, the fluence ratios $F_{TR\,red/blue}^{red/blue}(\mathbf{k}_l)$ and selectivity ratios $S_{TR}^{red/blue}(\mathbf{k}_l)$ for nanolocalization were determined and are represented as polar plots in Fig. 8b, c, respectively. Most of the fluence ratios are larger than one, and thus the back-propagated energy is preferentially directed to both emitter nanoparticles. The most efficient nanolocalization is found for illumination along the *x*-direction for emitter *red* and along a direction almost perpendicular for emitter *blue*. The angular distributions of $F_{TR\,red/blue}^{red/blue}(\mathbf{k}_0)$ indicate that two differently oriented dipolar resonances are responsible for efficient nanolocalization.

To assess the time reversal strategy, the selectivity ratios are more meaningful. Although, for nine out of ten illumination directions, the *TR blue* pulse causes higher fluence ratios for emitter *blue* than for emitter *red*, actual nanolocalization switching can only be achieved for four directions. In the polar projection of the selectivity ratio, one can now clearly point out the illumination directions for which time reversal succeeds in nanolocalization and nanolocalization switching is possible, i.e., $S_{TR}^{red} > 1$ and $S_{TR}^{blue} > 1$ are simultaneously fulfilled. This occurs for the illumination directions 0, 1, 4 and 9. Hence, only for four out of ten illumination directions localization switching and selective nano-addressing is possible. For the other directions, a switching of the local fluence between the emitter particles via time reversal is not possible.

The dipole pattern in the angular dependence of the fluence localization via time reversal indicates that local modes with a dipole characteristic are responsible for efficient nanolocalization. Accordingly, for particular illumination directions, the time reversal scheme allows for highly selective excitation of the two different emitters. However, for other directions, this selectivity is completely lost or even reversed. Hence, time reversal for unidirectional illumination does not provide a universal scheme for nanolocalization in the given random nanostructure.

Again, for the data shown in Fig. 8, the temporal evolution of the local electromagnetic fields is not taken into account. As it was discussed above for a particular

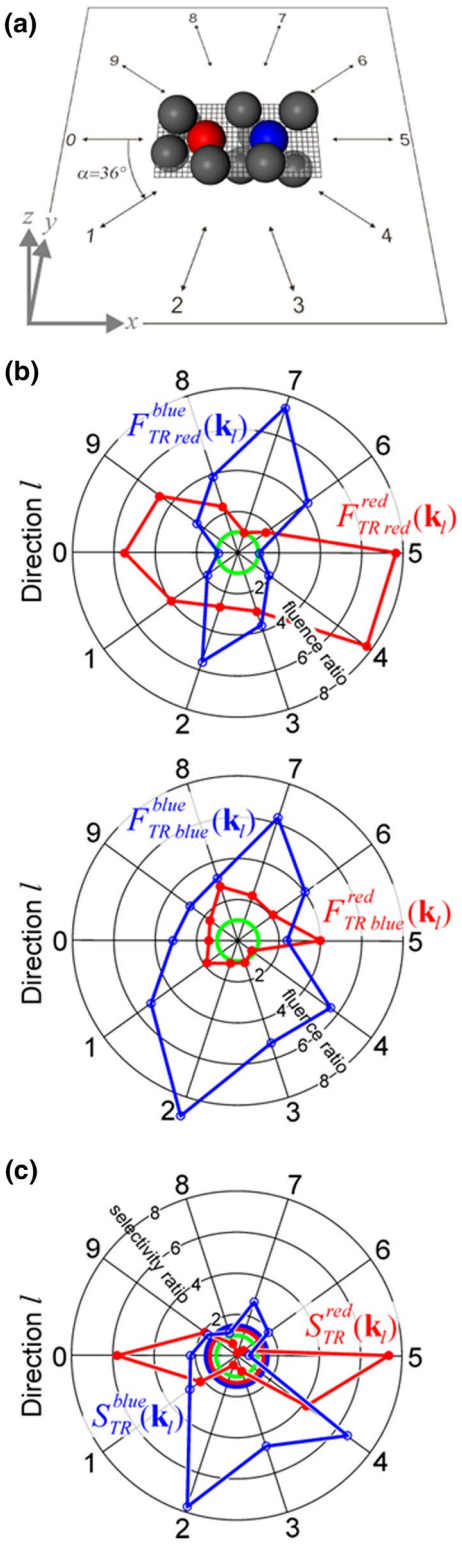

Fig. 8 Fluence and selectivity ratios for ten different illumination directions in the *xy*-plane. **a** 3D representation of the random scattering nanostructure with indicated plane wave illumination directions 0–9 in the *xy*-plane. **b** Fluence ratios $F^{red/blue}_{TR\,red/blue}(\mathbf{k}_l)$ for the different illumination directions $l = 0, 1, \ldots, 9$ for *TR red* and *TR blue* pulses as upper and lower polar diagram, respectively. **c** Selectivity ratios $S^{red/blue}_{TR}(\mathbf{k}_l)$ achieved by time reversal for different illumination directions in polar representation

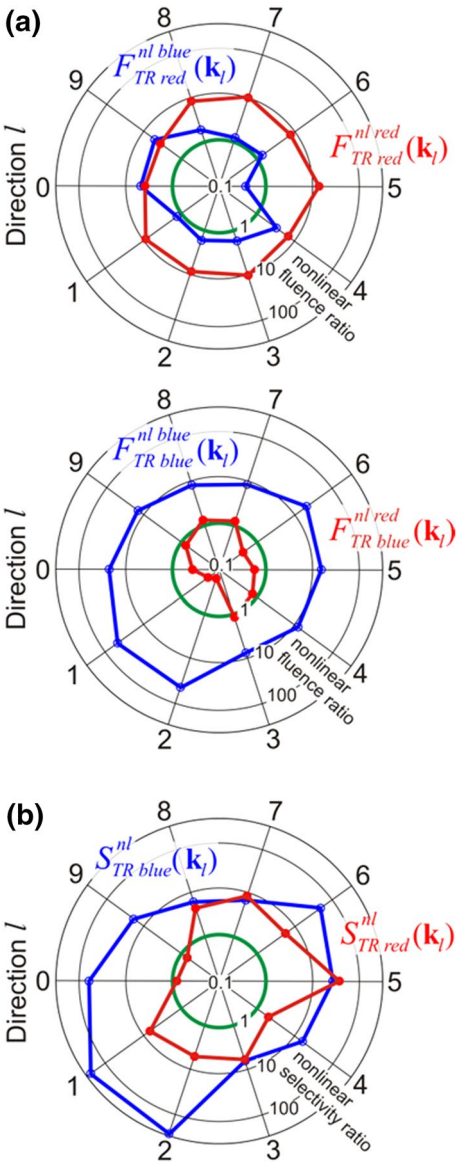

Fig. 9 Nonlinear fluence and selectivity ratios for ten different illumination directions in the *xy*-plane. **b** Nonlinear fluence ratios $F^{nl\,rot/blau}_{TR\,rot/blau}(\mathbf{k}_l)$ for the different illumination directions $l = 0, 1\ldots, 9$ for *TR red* and *TR blue* pulses as *left* and *right* polar diagram, respectively. **c** Nonlinear selectivity ratios $S^{nl}_{TR\,rot/blau}(\mathbf{k}_l)$ achieved by time reversal for different illumination directions in polar representation. Note the logarithmic radial scale in the polar plots

illumination direction, it is important to investigate the spatiotemporal focusing for the illumination from different directions. The corresponding nonlinear fluence $F^{nl}_{TR}(\mathbf{k}_l)$ and selectivity ratios $S^{nl}_{TR}(\mathbf{k}_l)$ are displayed in Fig. 9. For illumination with *TR red*, a predominant spatiotemporal localization at the emitter *red* occurs. Only for the illumination directions 0 and 9, a slightly higher nonlinear fluence at emitter *blue* is observed. For illumination with *TR blue*, the degree of spatiotemporal nanolocalization at emitter blue is even higher. The corresponding nonlinear selectivity

ratios $S_{TR}^{nl}(\mathbf{k}_l)$ shown in Fig. 9b reveal that for most illumination directions, the desired target emitter receives the higher nonlinear fluence. Interestingly, the orientation dependence of the selectivity ratio for the nonlinear fluence does not exhibit a clear dipolar characteristic. This indicates that the time reversal scheme for nanolocalization performs more reliably for nonlinear local signals. Hence, the behavior that was reported above for one particular illumination direction seems to hold for other illumination directions as well.

3.4 Spatial nanolocalization for cylindrical wave illumination

Until now interference between the time-reversed pulses of the different illumination directions has not been taken into consideration. But one might expect an enhancement for both nanolocalization via time reversal and adaptive optimization because of the additional degrees of freedom. In principle, perfect nanolocalization via time reversal can only be expected when the outgoing wave scattered in all directions is completely time-reversed, i.e., if the superposition of an infinite number of plane waves is considered. Hence not plane wave illumination for a single direction should be considered but a high order multipole expansion of the wavefront. A multipole expansion forms the natural basis to represent the outgoing and time-reversed wave since in the far field the random scattering nanostructure can be well conceived as a point emitter. However, we are not aware of any strategy to shape pulses in three dimensions in a multipolar basis. In contrast, polarization pulse shaping of different incident planar waves is possible although it is rather demanding and has to the best of our knowledge not yet been demonstrated experimentally. To more closely match the experimentally feasible time reversal scheme, we investigate a superposition of ten plane waves approximating a cylindrical wave illumination. For a better comparison and to reduce the computational cost, the ten directions investigated in the last subsection are used again here to represent the cylindrical wave.

Illumination with a time-reversed approximated cylindrical wave is achieved by coherent superposition of time-reversed fields for all ten illumination directions indicated in Fig. 8a. Again the local field contribution for each direction is given by Eq. 2 but now the total local field $\mathbf{E}_j^{local}(\mathbf{r}_i, \omega, cyl.)$ is the sum over the local fields for all illumination directions. Again adaptive optimization is used for comparison of nanolocalization efficiency. In this case, it is assumed that every direction contains unique information about the nanolocalization. Hence, in the adaptive optimization, the spectral phases for each illumination direction

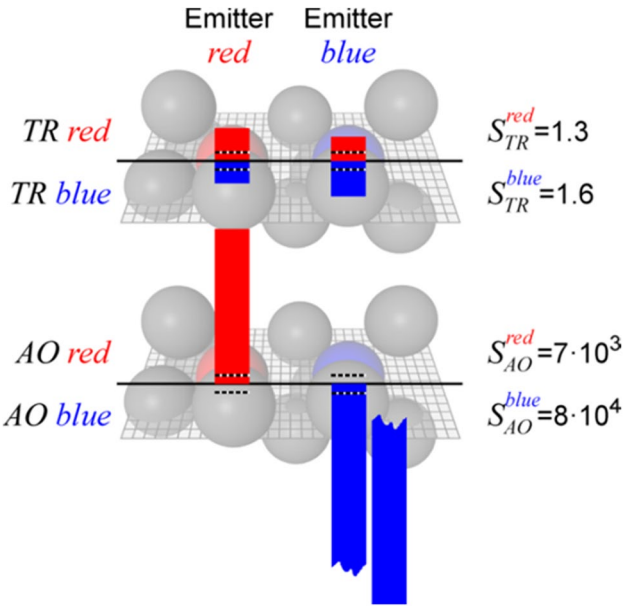

Fig. 10 Fluence ratios $F_j^{red/blue}$ and selectivity ratios $S_{TR/AO}^{red/blue}$ for cylindrical wave illumination for time reversal (*upper part*) and adaptive optimization nanolocalization (*lower part*). The cylindrical wave illumination is approximated by coherent superposition of ten planar waves propagating in the *xy*-plane as they are depicted in Fig. 8. The *dotted lines* represent the average fluence. The *bar* of the fluence ratio F_{AO}^{blue} is split for reasons of illustration

are independently varied leading to a tenfold enhancement of the phase space dimensionality. The fluence and selectivity ratios for both time reversal and the genetic algorithm are presented in Fig. 10.

Surprisingly, nanolocalization via time reversal of a cylindrical wave (Fig. 10, upper part) exhibits selectivity ratios only marginally above one for both emitters and hence the fluence ratios show only little contrast for both time-reversed pulses. Hence, no significant nanolocalization switching is achieved by time reversal. In contrast adaptive optimization yields several orders of magnitude larger selectivity ratios (Fig. 10, lower part) for both emitters. Accordingly, the additional degrees of freedom improve nanolocalization switching via adaptive optimization significantly, whereas it almost cancels nanolocalization switching via time reversal.

We associate the failure of the time reversal scheme with the directional averaging achieved by a cylindrical wave illumination. As seen in Fig. 8c, some directions show a large selectivity ratio, whereas other directions show a particularly small selectivity ratio. As discussed above, the directionality dependence exhibits a dipole characteristic and thus directional averaging cancels nanolocalization selectivity. In contrast, the adaptive scheme is immune against this directional averaging. The many degrees of freedom for the cylindrical wave illumination allow a

surprisingly efficient and highly selective nanolocalization of radiation.

3.5 Spatiotemporal nanolocalization for cylindrical wave illumination

Figure 11 summarizes the spatiotemporal nanolocalization behavior for cylindrical wave illumination. The distributions of the nonlinear fluence (Fig. 11c, f) exhibit moderate switching efficiency for time-reversed pulses and highly efficient nonlinear switching efficiencies for adaptively optimized nanolocalization. For two positions in the vicinity of the emitter particles, the temporal field amplitudes are presented (Fig. 11a, b, g, h). The same sampling positions as in Fig. 7 are chosen to calculate the average fluences $\langle f_j \rangle$ and thus a direct comparison of the nonlinear switching efficiency is possible. The *TR red* pulse induces an almost bandwidth-limited pulse of about 25 fs duration (FWHM) on emitter *red* (Fig. 11a). Note that the bandwidth limit here corresponds to the local field spectrum and thus is significantly longer than the original emitted pulse. On emitter *blue*, the peak intensity is about 5 times smaller (Fig. 11b) with again an almost bandwidth-limited temporal intensity profile. In contrast, the *TR blue* pulse generates temporally broadened intensities profiles of rather similar peak intensity (Fig. 11g). Furthermore, the fluence is homogenously distributed in the scattering structure with only little contrast between the active and inactive emitter (Fig. 11e). Accordingly, time-reversed pulses allow a highly selective spatiotemporal nanolocalization for emitter *red* but not for emitter *blue*. We conclude that in this nanostructure the time reversal scheme for spatiotemporal nanolocalization is applicable only by chance and does not provide a universal strategy to control spatiotemporal nanolocalization.

In contrast, as in the case for unidirectional illumination, the adaptive optimization scheme provides a very efficient method to flexibly control the spatiotemporal field evolution within a complex random nanostructure. The contrast in the nonlinear fluence between the active and inactive emitter is in the order of 10^3. The genetic algorithm also achieves almost bandwidth-limited temporal profiles for both emitters. Compared to unidirectional illumination, the additional degrees of freedom significantly enhance the nonlinear switching contrast. Interestingly, the random scattering nanostructure allows simultaneous control of spatial and temporal properties of the field distribution with a much higher contrast compared to the simpler structures

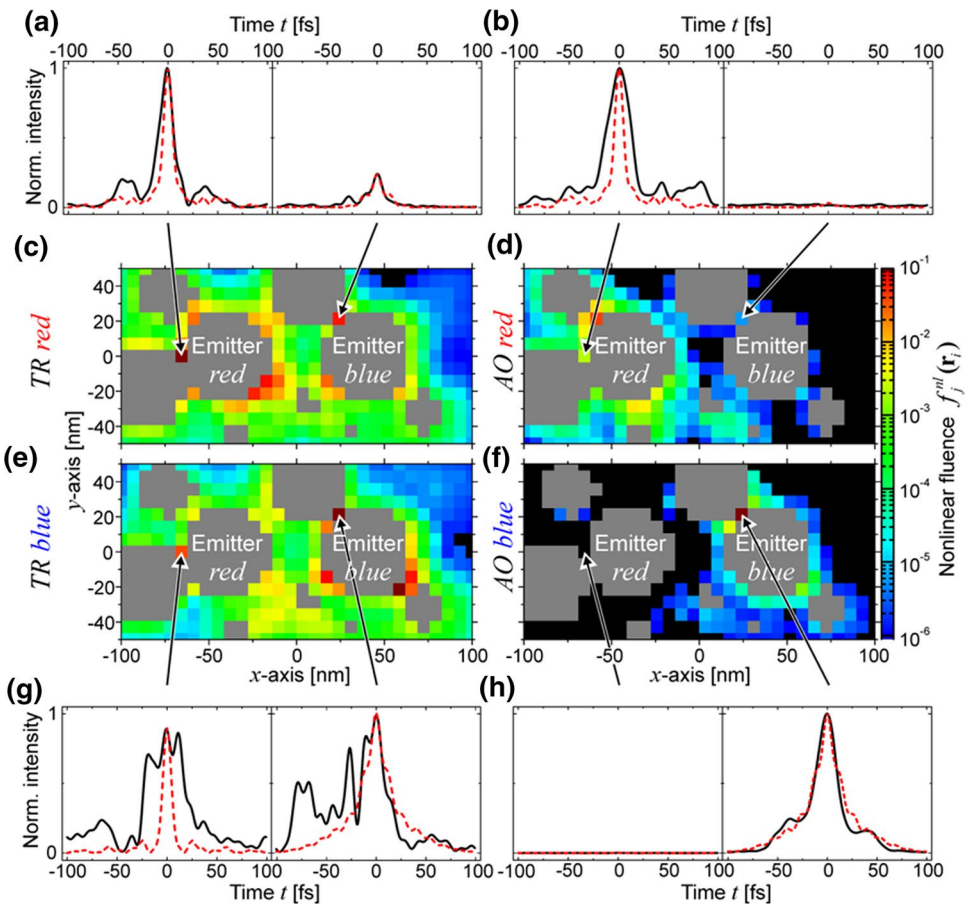

Fig. 11 Local time-resolved intensity (**a**, **b**, **g**, **h**) and local nonlinear fluence distribution (**c**, **d**, **e**, **f**) for nanolocalization via time reversal (part **a**, **c**, **e**, **g**) and adaptive optimization (part **b, d, f, h**) for approximate cylindrical wave illumination. For two representative points in the vicinity of each emitter as indicated by *arrows*, the time-dependent intensity is shown for time reversal (**a**, **g**) and adaptive optimization (**b**, **h**) normalized to the maximum peak intensity in *each panel*. For comparison, the bandwidth-limited local field intensity is shown as *red dashed line* normalized to each corresponding intensity *curve*

studied up to now in theoretical simulations [6, 7, 28–30] or experiments [8, 9].

3.6 Fluence nanolocalization for wave mixing reverberation chamber

According to the investigations presented up to now, neither plane nor cylindrical wave illumination leads to a reliable nanolocalization in the investigated random nanostructure. One possible explanation for this failure is still the possibility that indeed all scattered wave components need to be recorded and time-reversed. The successful demonstration of nanolocalization in the RF domain [17] achieves this by embedding the emitter and scattering structure in a reverberation chamber. The wave scattered in all directions is kept inside the reverberation chamber and eventually hits the receiver antenna array. Effectively this translates the information about the direction of the scattered wave components into the time domain since the different possible trajectories in the reverberation chamber require different propagation times until the wave hits the receiver antenna. Furthermore, information about directionality is also encoded since an array of receiver antennas is used—the so-called time reversal mirror. The scheme relies on subwavelength RF antennas and the ability to directly measure the local fields using fast electronic transient recorders. Unfortunately, this concept is not directly applicable for visible light, since no such subwavelength devices for electronic field detection are available at optical frequencies.

One possibility to mimic the behavior of the reverberation chamber is depicted in Fig. 12a. The nanostructure is placed inside a spherical cavity that has an open aperture. The nanostructure is placed off-center to avoid direct backpropagation of the outgoing wave onto the nanostructure after reflection at the cavity walls. The cavity itself is formed of a hollow gold metal sphere with a wall thickness of 200 nm. Light emitted from the electric dipoles embedded inside the nanostructure and scattered into various directions is reflected at the cavity walls, and eventually the light is emitted from the cavity via the aperture and detected in the far field at $\mathbf{r} = (0, -2.9, 0)$ µm. The size of the aperture is larger than the diffraction limit, and thus the light is efficiently transmitted to far-field modes outside the reverberation chamber. In fact it is large enough that the transmission efficiency varies by less than 10 % across the investigated frequency range (1.9–2.7 rad fs^{-1}). Hence, the wavelength selectivity of the aperture is neglected in the time reversal simulation. For the given geometry, the MESME code is not applicable and we used FDTD calculations to solve Maxwell's equations for this geometry (for details see Sect. 2).

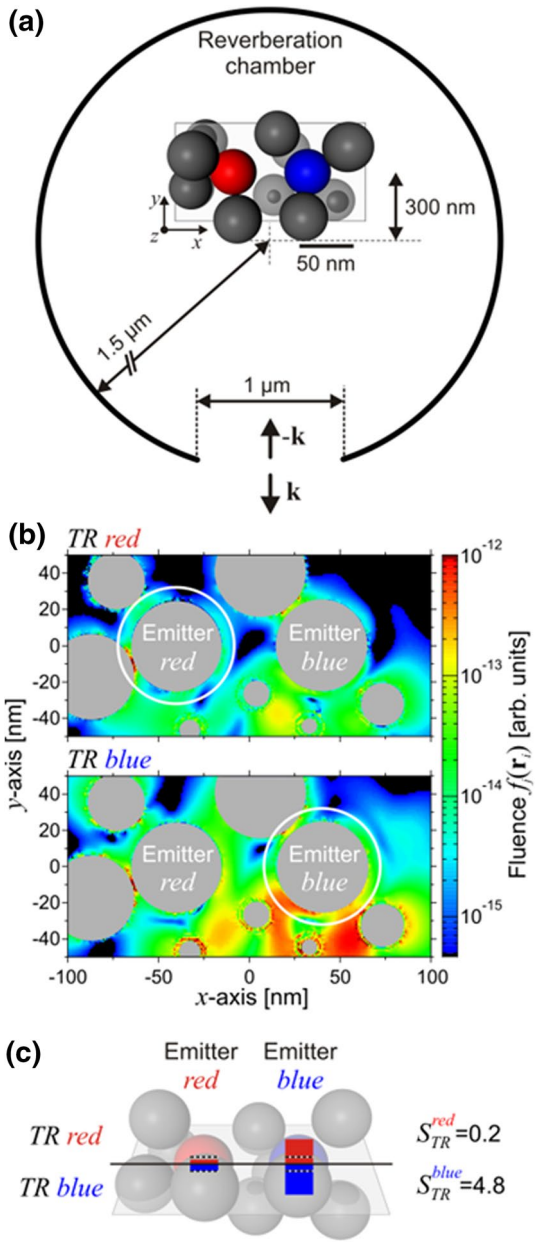

Fig. 12 Nanolocalization via time reversal for random scattering nanostructure embedded in a reverberation chamber. **a** Schematic representation of the geometry of reverberation chamber, aperture and embedded scattering nanostructure. **b** Local fluence distributions $f_j(\mathbf{r}_i)$ in the *xy*-plane of the scattering nanostructure obtained via time reversal are shown in log scale for illumination with the time-reversed field originally emitted from emitter *red* and *blue* as *upper* and *lower part* of the figure. The *white circle* borders the grid points that are inside a 32 nm radius around the emitter. The intersections with nanoparticles are *shaded* in *gray*. **c** Fluence ratios $F_j^{red/blue}$ and localization selectivity ratios $S_{TR}^{red/blue}$ for illumination with a plane wave through the hole of the reverberation chamber. For calculating these ratios, the same grid points as in the case without reverberation chamber are used

The wave emitted from the reverberation chamber is detected far from the aperture on the *y* axis. To calculate the nanolocalization via time reversal, the whole structure is then illuminated by a plane wave propagating in *y*-direction with spectral amplitudes and phases for both polarization components given by Eq. 1. Note that the illumination with a plane wave is a not reproducing the exact time-reversed wave since the wave emitted from the aperture does not have a planar wave front. The choice of using a plane wave illumination for the time-reversed propagation is motivated by the possibility for an experimental realization. The preparation of a complex polarization-shaped pulse with a controlled time-dependent non-planar wave-front evolution is beyond the means of present pulse shaping technology.

The resulting local fluence distributions are shown in Fig. 12b. In the vicinity of the nanoparticles, some small artifacts due to the staircasing effect in FDTD calculations are seen. However, a grid resolution was chosen for which the overall field distribution remains stable upon further decrease of the cell size. For the *TR blue* pulse, in general, a higher local fluence is observed compared to *TR red* illumination. However, the local fluence patterns show now clear differences for both time-reversed fields. This is also reflected in the fluence and selectivity ratios (Fig. 12c). A selective nanolocalization is observed only for the *TR blue* pulse. In case of TR red illumination, even more energy is directed to emitter *blue* than to emitter *red*. Hence, both selectivity ratios are not simultaneously above unity and a selective addressing of both emitters by time-reversed fields is not possible.

Note that illumination from the *y*-direction yields small selectivity ratios also for the plain scattering nanostructure (Fig. 8c, direction $l = 7$ or 8). This is not improved by the presence of the reverberation chamber. Hence, the reverberation chamber in its present realization does not significantly influence the nanolocalization via time reversal. In the present investigation, little differences are observed in the achieved localization selectivity for either plane wave or cylindrical wave illumination, and embedding the scattering structure in a reverberation chamber. From this, we conclude that the degree to which different outgoing wave components are taken into account to determine the time-reversed field has no significant impact on the localization selectivity.

4 Discussion

The first theoretical demonstration of the time reversal scheme in nanooptics was performed for surface plasmon polariton waves propagating on a thin metallic wedge [20] and could give a hint on the requirements for successful applications of the time reversal scheme. Surface plasmon polaritons wavepackets are launched on the side planes of a metallic wedge with optimal spectral phase and amplitude so that the superimposed propagating fields focus in space and time on the knife edge. In this particular case, the initial conditions for the surface plasmon polaritons wavepackets were obtained from back-propagating the ultrashort nanolocalized field distribution starting from the knife edge, i.e., by time reversing the desired control goal [20]. In this case, pure wave propagation is involved and multiple scattering plays no role. This is in strong contrast to the present investigation where strong scattering in the nanostructure occurs.

In the random nanostructure investigated here, the time reversal scheme in general fails to selectively nanolocalize the incident radiation at distinct randomly chosen positions in the nanoscale scattering environment. On a first glimpse, this seems to contradict the reported nanolocalization in a two-dimensional random nanostructure reported by Li and Stockman [21]. However, it is important to note that in this study the emitter position was not chosen randomly but placed at a strong local resonance providing good coupling to the far field. If this is by chance fulfilled in the structure investigated here, we also see a reasonably good nanolocalization. If the emitter position is coupled to a local mode, a reverberation chamber as it is used in the RF nanolocalization experiment [17] is dispensable or even counter-productive.

A still open question is the role of dissipation in nanolocalization of time-reversed fields. In case of strong absorption, it is obvious that the outgoing wave is distorted by absorption. Actually the frequency components initially coupled to a strong local mode might be absorbed locally and are thus not radiated to the far field at all. In the present investigation, we have intentionally chosen core–shell particles to minimize absorption. Hence we do not expect that the random nanoantenna investigated here operates in the limit of strong absorption. In the course of the investigation, also aggregates composed of metal nanoparticles that exhibit a stronger absorption were investigated. Also for these structures, no reliable nanolocalization via time reversal was obtained. This leaves the further reduction of absorption in the random nanoantenna is an interesting route for further studies.

A recent theoretical investigation of acoustic waves in a medium with a low density of randomly distributed bubbles [25] sheds more light on possible reasons for the failure of the time reversal scheme in the present case. Multiple scattering calculations show that nanolocalization via time reversal is only achieved in a spectral domain that does not overlap with resonances of the scattering particles, i.e., in this case the bubbles. Extrapolating this finding to the optical regime indicates that the choice of more or less resonant core–shell particles (compare Fig. 1b) might

be disadvantageous. Still it is important to note that the mode spectrum of the medium is composed of sharp resonances. This indicates that still resonant modes in the scattering play an important role, but these seem to be modes appearing because of nonresonant scattering. We expect that adopting the conditions for this acoustic nanolocalization to electromagnetic waves in random media might boost the time reversal scheme. To achieve this, it seems essential that the balance between scattering and absorption is optimized. Introducing hierarchical scattering structures composed, for example, of nanoparticle dimers interacting with each other with adjustable strength or highly scattering dielectric nanostructures might open interesting pathways toward successful nanolocalization of optical fields via time reversal.

The rather surprising finding of our investigation is the highly efficient nanolocalization and excitation selectivity achieved via adaptive near-field optimization. Even in cases when the time reversal scheme completely fails the random nanostructure can act as a highly selective nanoantenna if the appropriate polarization-shaped illumination pulse is used. This emphasizes and confirms that polarization shaping is essential to achieve a high spatial selectivity and temporal control in nanolocalization [7]. The spatial selectivity achieved in this random nanostructure by adaptive pulse shaping is significantly improved compared to previously investigated more regular structures [7, 29, 30]. Identification of the reasons for this high selectivity requires investigating an ensemble of different random nanostructure to establish statistically significant conclusions concerning the nanolocalization selectivity. This is beyond the scope of the present investigation. However, the fact that a random nanostructure acts as a highly selective optical nanoantenna sheds light on the relevance of random structures in photonics [31]. Random structures can provide a vast number of localized modes, scattering pathways, and intricate coupling phenomena leading to very interesting properties. In the context of adaptive control, it is interesting to note, that randomly nanotextured interfaces exhibit striking properties that are related to rather long-lived photonic states [32–34]. Seemingly, random nanoantennas exhibit by chance functionalities that outperform dedicated structures. This is nicely demonstrated by Feichtner et al. in an adaptive optimization of a random nanoantenna leading to the identification of a highly efficient new optical antenna design [35].

5 Conclusion

We have compared time reversal and adaptive optimization to control the spatial and temporal evolution of electromagnetic fields localized on subwavelength scale with in a random scattering nanostructure. Although nanolocalization via time reversal is already demonstrated successfully for acoustic and RF fields, it proved rather inefficient for the investigated nanostructure. In contrast, adaptive optimization performed surprisingly well and in all cases superior nanolocalization efficiency and selectivity is reported. The comparison of different realizations of the time reversal scheme showed that partial capturing of the outgoing wave is not responsible for its failure. Even embedding the nanostructure in an “open” reverberation chamber acting as directional mode compressor does not enable nanolocalization via time reversal. The comparison of nanolocalization via time reversal for different illumination directions indicates that the coupling of the target emitter to local dipolar modes determines the effectiveness of the time reversal scheme. The surprisingly efficient selective nanolocalization via adaptive optimization demonstrates that random nanoantenna designs are interesting objects to achieve small-scale high contrast multiplexing devices.

Acknowledgments This work was supported by the German Science Foundation (DFG) within the SPP 1391. We thank Javier García de Abajo for helpful discussions and for making the MESME code available for the shown field calculations.

References

1. P. Biagioni, J.-S. Huang, B. Hecht, Nanoantennas for visible and infrared radiation. Rep. Prog. Phys. **75**(2), 024402 (2012)
2. J.S. Huang, T. Feichtner, P. Biagioni, B. Hecht, Impedance matching and emission properties of nanoantennas in an optical nanocircuit. Nano Lett. **9**(5), 1897–1902 (2009)
3. T.H. Taminiau, F.D. Stefani, F.B. Segerink, N.F. van Hulst, Optical antennas direct single-molecule emission. Nat. Photon. **2**(4), 234–237 (2008)
4. M. Richter, F. Schlosser, M. Schoth, S. Burger, F. Schmidt, A. Knorr, S. Mukamel, Reconstruction of the wave functions of coupled nanoscopic emitters using a coherent optical technique. Phys. Rev. B **86**(8), 085308 (2012)
5. M.I. Stockman, S.V. Faleev, D.J. Bergman, Coherent control of femtosecond energy localization in nanosystems. Phys. Rev. Lett. **88**(6), 067402 (2002)
6. T. Brixner, F.J. García de Abajo, J. Schneider, W. Pfeiffer, Nanoscopic ultrafast space-time-resolved spectroscopy. Phys. Rev. Lett. **95**(9), 093901 (2005)
7. T. Brixner, F.J. García de Abajo, J. Schneider, C. Spindler, W. Pfeiffer, Ultrafast adaptive optical near-field control. Phys. Rev. B **73**(12), 125437 (2006)
8. M. Aeschlimann, M. Bauer, D. Bayer, T. Brixner, F.J. García de Abajo, W. Pfeiffer, M. Rohmer, C. Spindler, F. Steeb, Adaptive subwavelength control of nano-optical fields. Nature **446**, 301–304 (2007)
9. M. Aeschlimann, M. Bauer, D. Bayer, T. Brixner, S. Cunovic, F. Dimler, A. Fischer, W. Pfeiffer, M. Rohmer, C. Schneider, F. Steeb, C. Strüber, D.V. Voronine, Spatiotemporal control of nanooptical excitations. Proc. Natl. Acad. Sci. USA **107**(12), 5329–5333 (2010)
10. R.J. Potton, Reciprocity in optics. Rep. Prog. Phys. **67**(5), 717–754 (2004)

11. A. Derode, P. Roux, M. Fink, Robust acoustic time reversal with high-order multiple scattering. Phys. Rev. Lett. **75**(23), 4206 (1995)
12. M. Fink, D. Cassereau, A. Derode, C. Prada, P. Roux, M. Tanter, J.L. Thomas, F. Wu, Time-reversed acoustics. Rep. Prog. Phys. **63**(12), 1933–1995 (2000)
13. G.F. Edelmann, T. Akal, W.S. Hodgkiss, S. Kim, W. Kuperman, H.C. Song et al., An initial demonstration of underwater acoustic communication using time reversal. IEEE J. Ocean. Eng. **27**(3), 602–609 (2002)
14. M. Fink, Time-reversed acoustics. Sci. Am. **281**(5), 91–97 (1999)
15. G. Lerosey, J. de Rosny, A. Tourin, A. Derode, G. Montaldo, M. Fink, Time reversal of electromagnetic waves. Phys. Rev. Lett. **92**(19), 193904 (2004)
16. G. Lerosey, J. de Rosny, A. Tourin, A. Derode, M. Fink, Time reversal of wideband microwaves. Appl. Phys. Lett. **88**(15), 154101 (2006)
17. G. Lerosey, J. de Rosny, A. Torin, M. Fink, Focusing beyond the diffraction limit with far-field time reversal. Science **315**(5815), 1120–1122 (2007)
18. R. Carminati, J.J. Saenz, J.-J. Greffet, M. Nieto-Vesperinas, Reciprocity, unitarity, and time-reversal symmetry of the S matrix of fields containing evanescent components. Phys. Rev. A **62**(1), 012712 (2000)
19. R. Carminati, R. Pierrat, J. de Rosny, M. Fink, Theory of the time reversal cavity for electromagnetic fields. Opt. Lett. **32**(21), 3107–3109 (2007)
20. M. Durach, A. Rusina, M.I. Stockman, K.A. Nelson, Toward full spatiotemporal control on the nanoscale. Nano Lett. **7**(10), 3145–3149 (2007)
21. X. Li, M.I. Stockman, Highly efficient spatiotemporal coherent control in nanoplasmonics on a nanometer-femtosecond scale by time reversal. Phys. Rev. B **77**(19), 195109 (2008)
22. F.J. García de Abajo, Multiple scattering of radiation in clusters of dielectrics. Phys. Rev. B **60**(8), 6086–6102 (1999)
23. U.K. Chettiar, N. Engheta, Internal homogenization: effective permittivity of a coated sphere. Opt. Express **20**(21), 22976 (2012)
24. P.B. Johnson, R.W. Christy, Optical constants of the noble metals. Phys. Rev. B **6**(12), 4370–4379 (1972)
25. M. Lanoy, R. Pierrat, F. Lemoult, M. Fink, V. Leroy, A. Tourin, Subwavelength focusing in bubbly media using broadband time reversal. Phys. Rev. B **91**(22), 224202 (2015)
26. T. Brixner, Poincaré representation of polarization-shaped femtosecond laser pulses. Appl Phys B **76**(5), 531–540 (2003)
27. W. Pfeiffer, M. Aeschlimann, T. Brixner, Coherent control of nano-optical excitations, in *Optical Antennas*, ed. by M. Agio, A. Alú (Cambridge University Press, Cambridge, 2013), pp. 145–167
28. M.I. Stockman, Ultrafast nanoplasmonics under coherent control. New J. Phys. **10**, 025031 (2008)
29. M. Sukharev, T. Seideman, Coherent control of light propagation via nanoparticle arrays. J. Phys. B: At. Mol. Opt. Phys. **40**(11), S283–S298 (2007)
30. P. Tuchscherer, D.V. Voronine, C. Rewitz, F.J. García de Abajo, W. Pfeiffer, T. Brixner, Analytic control of plasmon propagation in nanostructures. Opt. Express **17**(16), 14235–14259 (2009)
31. D.S. Wiersma, Disordered photonics. Nat. Photon. **7**(3), 188–196 (2013)
32. M. Aeschlimann, T. Brixner, A. Fischer, C. Kramer, P. Melchior, W. Pfeiffer, C. Schneider, C. Strüber, P. Tuchscherer, D.V. Voronine, Coherent two-dimensional nanoscopy. Science **333**(6050), 1723–1726 (2011)
33. M. Aeschlimann, T. Brixner, S. Cunovic, A. Fischer, P. Melchior, W. Pfeiffer, M. Rohmer, C. Schneider, C. Strüber, P. Tuchscherer, D.V. Voronine, Nanooptical control of hot-spot field superenhancement on a corrugated silver surface. IEEE J. Sel. Top. Quantum Electron. **18**(1), 275–282 (2012)
34. M. Aeschlimann, T. Brixner, D. Differt, U. Heinzmann, M. Hensen, C. Kramer, F. Lükermann, P. Melchior, W. Pfeiffer, M. Piecuch, C. Schneider, H. Stiebig, C. Strüber, P. Thielen, Perfect absorption in nanotextured thin films via Anderson-localized photon modes. Nat. Photon. **9**(10), 663–668 (2015)
35. T. Feichtner, O. Selig, M. Kiunke, B. Hecht, Evolutionary optimization of optical antennas. Phys. Rev. Lett. **109**(12), 127701 (2012)